

Supplementary Material:

Manipulating Topological Valley Modes in Plasmonic Metasurfaces

Matthew Proctor, Paloma A. Huidobro, Stefan A. Maier,
Richard V. Craster, Mehul P. Makwana

December 2, 2019

S1 Coupled Dipole Method

The coupled dipole method (CDM) is used to model interactions between nanoparticles (NPs). For each lattice arrangement we assume that the NP radius r , nearest neighbour spacing R , and lattice constant a_0 are all sub-wavelength. Furthermore, we ensure that $R > 3r$ which allows the NPs to be treated as point dipoles, as higher order resonances can be neglected [1]. The optical response of the NPs is described by the polarisability $\alpha(\omega)$. We use the modified long wavelength approximation (MLWA) which accurately models [spheroidal](#) metal NPs including radiative effects [2],

$$\alpha_{\text{MLWA}}(\omega) = \frac{\alpha_s(\omega)}{1 - \frac{k^2}{l_E} D \alpha_s(\omega) - i \frac{2k^3}{3} \alpha_s(\omega)}. \quad (1)$$

k is the wavenumber, l_E is the spheroid major axis length and D is a dynamic geometrical factor. The static polarisability $\alpha_s(\omega)$ is given by,

$$\alpha_s(\omega) = \frac{V}{4\pi} \frac{\epsilon(\omega) - 1}{1 + L(\epsilon(\omega) - 1)}, \quad (2)$$

where V is the NP volume and L is a static geometrical factor. The geometrical factors D and L are dependent on the size and shape of the spheroid. For a sphere, components of L and D will be the same in all axes, respectively. For a spheroid, the geometrical factors are split into components along the longest axis L_z and the axes perpendicular to this L_x and L_y . Since we only consider out-of-plane dipole moments, we only require L_z . The static geometrical factor L_z for a prolate spheroid (where the height is larger than the diameter) is,

$$L_z = \frac{1 - e^2}{e^3} (-e + \arctan he), \quad (3)$$

where e is the eccentricity,

$$e^2 = \frac{h^2 - 4r^2}{h^2}. \quad (4)$$

The dynamic geometrical factor D_z is,

$$D_z = \frac{3}{4} \times \frac{1 + e^2}{1 - e^2} L_z + 1, \quad (5)$$

The other components L_{xy} and D_{xy} , for the in-plane polarisabilities, can be determined from the sum rules detailed in Ref. [2]. We assume the NPs are in vacuum.

The interaction between multiple NPs is described by the Green's function. For two particles at positions \mathbf{r}_i and \mathbf{r}_j , the Green's function for out-of-plane dipole moments is given by,

$$G_{zz}(\mathbf{r}_i - \mathbf{r}_j, \omega) = e^{ikr} \left(\frac{k^2}{r} + \frac{ik}{r^2} - \frac{1}{r^3} \right), \quad (6)$$

where $k = \omega/c$ is the wavenumber and $r = |\mathbf{r}_i - \mathbf{r}_j|$.

For a periodic lattice we apply Bloch's theorem and arrive at the following eigenvalue problem,

$$\hat{\mathbf{H}}(\mathbf{q}, \omega) \cdot \mathbf{p} = \frac{1}{\alpha(\omega)} \mathbf{p}, \quad (7)$$

with Bloch wavevector \mathbf{q} . The **interaction matrix** $\hat{\mathbf{H}}(\mathbf{q}, \omega)$ has elements,

$$H_{ij} = \begin{cases} \sum_{\mathbf{R}} G_{zz}(\mathbf{r}_i - \mathbf{r}_j + \mathbf{R}, \omega) e^{i\mathbf{q} \cdot \mathbf{R}} & i \neq j \\ \sum_{|\mathbf{R}| \neq 0} G_{zz}(\mathbf{R}, \omega) e^{i\mathbf{q} \cdot \mathbf{R}} & i = j \end{cases}, \quad (8)$$

where the indices i, j run from 1 to the total number of NPs in the unit cell. Each component of the **interaction matrix** has a summation running over neighbouring unit cells. In the bulk band structures in Fig 2 and the ribbon band structures in Fig 5, 6, we use the QSA when calculating the bulk and ribbon band structures. Rather than only using nearest neighbours in the QSA, we include all neighbours to give a more physical description of the system. The lattice sums converge quickly in the QSA, but a numerical artefact of this method is the discontinuity at Γ for some bands, owing to the group velocity v_g necessarily equalling zero here [3].

The spectral function plots in Fig 2 and Fig 3 rely on an effective polarisability model and involve lattice sums with the full Green's function in Equation 6. These only converge conditionally and additional manipulation is required to converge them [4]. Unlike the QSA, the spectral function captures the effects of retardation and radiation.

To set up the scattering problem, we use the full three-dimensional Green's function to ensure the multiple scattering between NPs is modelled appropriately. We set up a $3N \times 3N$ matrix for N NPs and excite the system with a magnetic dipole, in order to excite the out-of-plane dipole modes.

S2 Symmetry arguments for the existence of Dirac cones

As we described in the main text, K/K' support Dirac cones if they have point group symmetry $C_{3v} = C_3 + 3\sigma_v$, i.e. $G_{K/K'} = C_{3v}$. Where σ_v corresponds to vertical mirror symmetry. From this we can determine the symmetry at Γ (G_Γ), since C_{3v} is a normal subgroup of G_Γ this implies, $G_\Gamma = C_{6v}$ or C_{3v} . The C_{6v} case is analogous to existing graphene-like structures. For completeness, we also note that K/K' will also support Dirac cones for $G_{K/K'} = C_3$ but if and only if $G_\Gamma = C_6$ [5]. The three cases in full are $\{G_{K/K'}, G_\Gamma\} = \{C_{3v}, C_{6v}\}, \{C_{3v}, C_{3v}\},$ or $\{C_3, C_6\}$. In order to gap the Dirac cone, and create two inequivalent K, K' valleys, $G_{K/K'}$ must be reduced down to C_3 . Removing σ_v opens the Dirac cone in the $\{C_{3v}, C_{3v}\}$ case and for the other two cases, we must break inversion symmetry to further reduce the point group symmetry G_Γ to C_3 . Whilst Dirac cones are guaranteed for the symmetries described above, they can also be engineered in systems with other symmetries, such as the square C_{4v} symmetry. The degeneracies for this lattice structure are not entirely symmetry-induced but their presence is not restricted by symmetry-based band repulsion [6].

S3 Emergence of topological valley modes in a C_{4v} system

Using a square lattice structure with C_{4v} symmetry, shown in Figure S1A, we are able to engineer Dirac cones along XM and XN in the BZ, Figure S1C. The Dirac cones obtained exist along high-symmetry lines as opposed to high-symmetry points. There are three lower energy bands not shown, as they are not in the vicinity of the Dirac cone. We note that the existence, and location, of Dirac cones is dependent on the system and they would not necessarily exist, say, for any simple square lattice structure therefore it is interesting to observe their presence for our system parameters. A limitation of the C_{4v} case for this particular system, however, is the small band gap which limits potential applications.

As with the C_{3v} and C_{6v} Type I cases in the main text, edge states are anticipated between regions with perturbations $+\theta$ and $-\theta$, respectively. However, unlike those cases, now both parity edge modes exist along the same interface. Here A/B and B/A interfaces are identical (modulo time-reversal symmetry) which means that a mode propagating to the left (right) on an A/B interface is identical to a right (left) propagating mode on a B/A interface. This has implications for the splitting of modes along these interfaces.

We set up scattering calculations in order to investigate the propagation of modes in the C_{4v} system. Losses are detrimental to the existence of edge states in this system, owing to the small band gap. We therefore model the system with zero Drude losses to highlight the potential of edge states in systems with C_{4v} symmetry. In Figure S2A, we show the mode propagating around a $\pi/2$ bend. The Fabry-Pérot like behaviour of the leads suggests that we require a minimum in the energy-carrying envelope at the corner to maximise propagation [6], since the corner acts as a reflector. We show this by calculating the transmission through a plane perpendicular to both the interface and the metasurface before and after the corner, in Figure S2C. The propagation around the corner is not as robust as the C_{3v} and C_{6v} systems due to the smaller Fourier separation, and hence transmission is smaller.

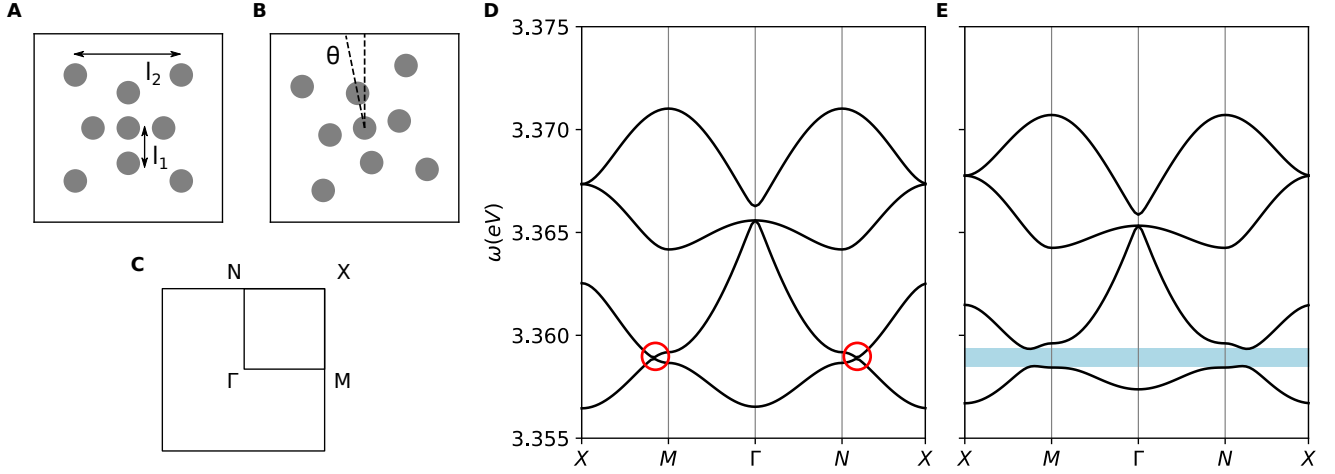


Figure S1: C_{4v} case: (A) Unit cell with spherical NPs, radius $r = 5$ nm, internal spacing $l_1 = 15$ nm, external spacing $l_2 = 45$ nm, lattice constant $a_0 = 80$ nm, (B) A $\theta = 0.3$ rad rotation removes σ_v , (C) BZ, (D) Band structure, pre-perturbation: The system has accidental degeneracies along XM and XN , (E) Post-perturbation.

In Figure S2B, we demonstrate three-way topological energy-splitting. To maximise the splitting along the other leads, it is now desirable to have a maximum displacement of the energy-carrying envelope at the junction. Notably, only two-way partitioning of energy is possible using the triangular lattice cases; this is also true if we were to consider armchair terminations. The identical nature of the A/B and B/A interfaces for this case allows for the third outgoing lead to be ignited. Despite the smaller Fourier separation, for this case, each of the outgoing modes preserve their topological charge thereby inheriting a layer of topological protection. Finally, in Figure S2D, we plot a cut plane perpendicular to the metasurface and the interface to highlight the subwavelength confinement of the mode in the z -direction.

S4 Additional waveguiding techniques with C_{3v} networks

A number of advanced techniques can be achieved with C_{3v} networks, however these effects are sensitive to excitation frequency. In Figure S4A we show C_{3v} , Type I edge states splitting four ways at a junction. The junction is chosen so that the mode travels without a barrier from lead 1 to lead 6. The decay of the mode perpendicular to this then ignites modes to propagate along the other four leads. This splitting is topologically robust since topological charge is preserved at the junction [7].

Trivial edge states are possible at the interface between regions of the same valley-Chern number. In this system, these occur when region A and B are perturbed by $+\theta$ and $-\theta - \frac{\pi}{3}$, respectively. In Figure S3 we show the band structure for C_{3v} , Type III edges. Despite being visually indistinguishable in the band structure, there are actually two nearly degenerate states in the band gap, due to the similarity between A/B and B/A interfaces. The eigenmodes at each interface are shown on either side.

The similarity between A/B and B/A interfaces means that there will always be a mode to couple to around a sharp ($\pi/3$) or gentle ($2\pi/3$) bend. In Figure S4B, we show C_{3v} , Type III edge states splitting five ways. This is the maximum possible number of ways to split a mode whilst keeping zig-zag interfaces on a triangular lattice. As in the four-way splitting with Type I edge states, the decay of the mode once it reaches the junction is used to trigger modes to propagate along the other leads. However, unlike those the Type I network this five-way splitting is not topologically protected. The Fourier separation between counter propagating modes provides enough protection for the modes to split in this way though. Since the edge state excited has a group velocity $v_g \approx 0$ as shown in the ribbon system, Figure S3, we see a beating of the mode.

Since the band gap of the C_{3v} system is smaller than the C_{6v} system, it is more susceptible to losses. In Figure S5 we plot the spectral function for the bulk system with Drude losses $\gamma = 38$ meV. Whilst the bands become very broad, they are still distinguishable. Additionally, in Figure S6 we plot the edge states for the Type I interface for $\gamma = 10$ meV. Again, although the edge states become broad due to radiative effects, it is still possible to distinguish them from the bulk. We highlight the edge states in white for clarity. In Figure S7, we simulate a C_{3v} Type I interface with smaller losses $\gamma = 5$ meV and 10 meV.

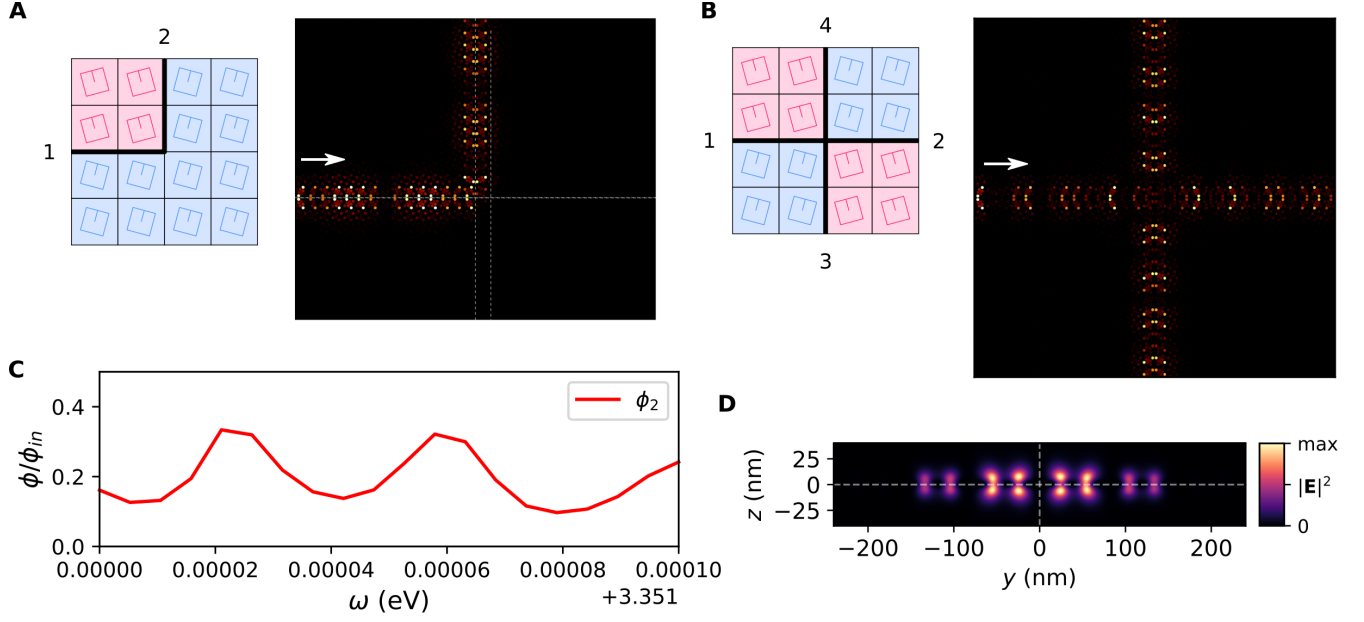


Figure S2: Waveguiding with C_{4v} networks. (A) Three-way splitting junction, $\omega = 3.351079$ eV. (B) $\pi/2$ corner, $\omega = 3.351$ eV, (C) Electric field intensity, $|\mathbf{E}|^2$ at a cut plane perpendicular to the interface and the metasurface, (D) Transmission ϕ through a plane perpendicular to lead 2 as a fraction of input transmission along lead 1. The resonance peaks indicate a Fabry-Pérot like behaviour.

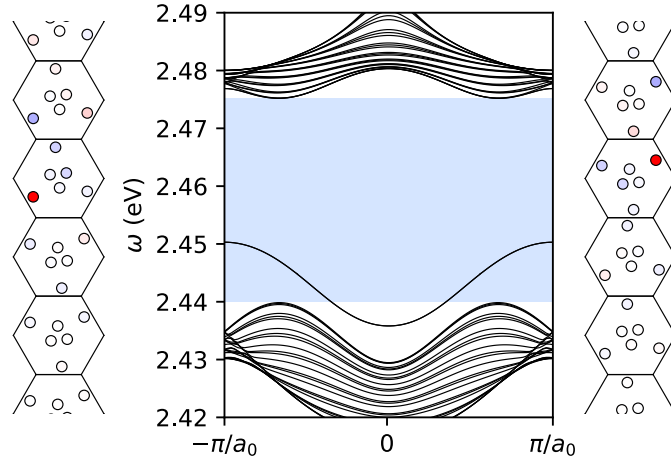


Figure S3: C_{3v} , Type III: The upper and lower media are perturbed by $\theta = +0.1$ rad and $\theta = -0.1 + \frac{\pi}{3}$ rad, respectively. The edge states are almost degenerate due to the similarity between the interface in real space. The dipole moments of each edge state are shown on either side.

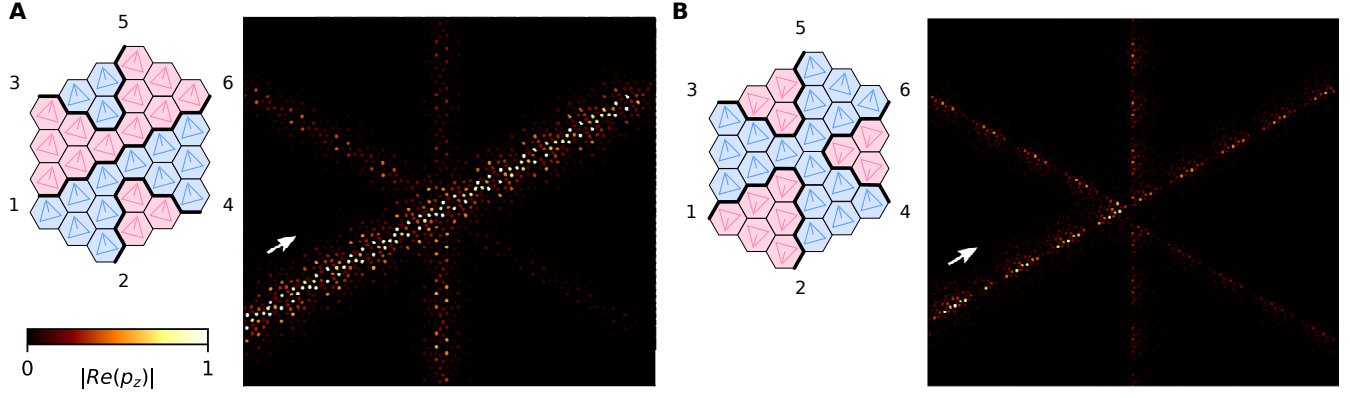


Figure S4: (A) Four-way splitting, C_{3v} , Type I, (B) Five-way splitting, C_{3v} , Type III.

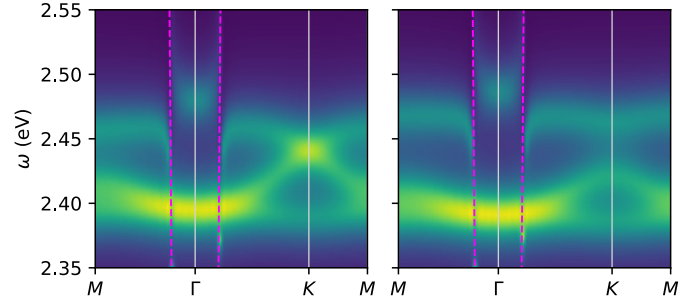


Figure S5: Spectral function for the C_{3v} lattice. Drude losses $\gamma = 38$ meV.

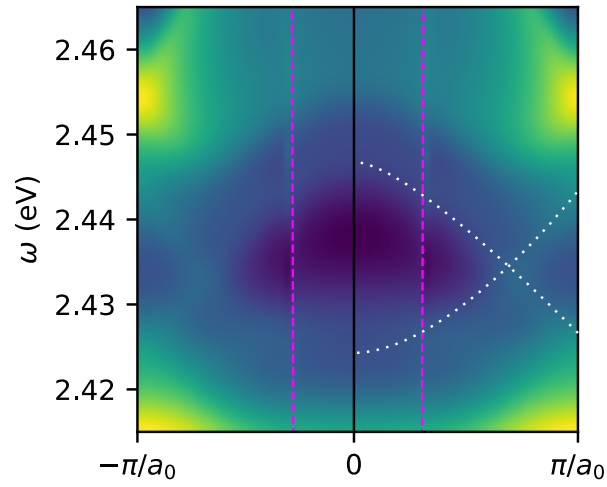


Figure S6: C_{3v} , Type I: Spectral function, $\gamma = 10$ meV. Edge states are highlighted in white.

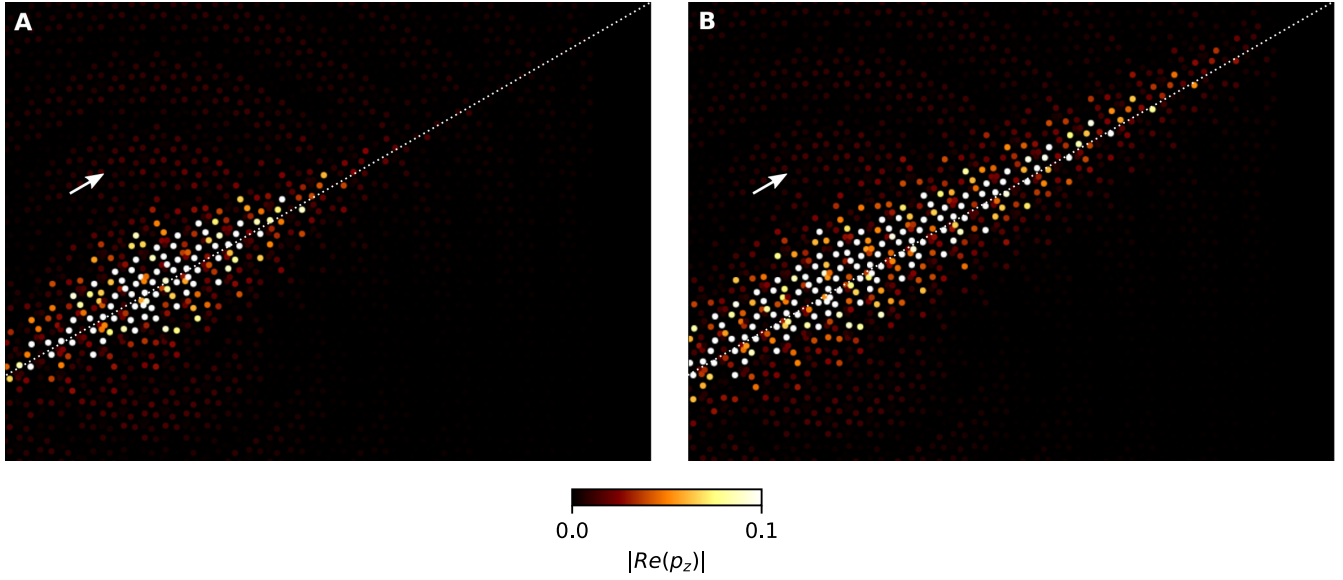


Figure S7: C_{3v} , Type I interface including losses, (A) $\gamma = 5$ meV, (B) $\gamma = 10$ meV.

References

- [1] W. Weber and G. Ford. “Propagation of optical excitations by dipolar interactions in metal nanoparticle chains”. *Phys. Rev. B* 70.12 (2004), p. 125429.
- [2] A. Moroz. “Depolarization field of spheroidal particles”. *JOSA B* 26.3 (2009), pp. 517–527.
- [3] Y.-R. Zhen, K. H. Fung, and C. Chan. “Collective plasmonic modes in two-dimensional periodic arrays of metal nanoparticles”. *Phys. Rev. B* 78.3 (2008), p. 035419.
- [4] C. M. Linton and I. Thompson. “One-and two-dimensional lattice sums for the three-dimensional Helmholtz equation”. *J. Comput. Phys.* 228.6 (2009), pp. 1815–1829.
- [5] M. P. Makwana and R. V. Craster. “Geometrically navigating topological plate modes around gentle and sharp bends”. *Phys. Rev. B* 98.18 (2018), p. 184105.
- [6] M. P. Makwana and G. J. Chaplain. “Tunable three-way topological energy-splitter: venturing beyond graphene-like structures”. *arXiv preprint arXiv:1901.01937* (2019).
- [7] M. Ezawa. “Topological Kirchhoff law and bulk-edge correspondence for valley Chern and spin-valley Chern numbers”. *Phys. Rev. B* 88.16 (2013), p. 161406.